

Multiscale Grassmann Manifolds for Single-Cell Data Analysis

Xiang Xiang Wang¹, Sean Cottrell^{1,2}, and Guo-Wei Wei^{1,3,4*}

¹ Department of Mathematics,

Michigan State University, East Lansing, MI 48824, USA.

² Department of Computational Mathematics, Science, and Engineering,

Michigan State University, East Lansing, MI 48824, USA.

³ Department of Biochemistry and Molecular Biology,

Michigan State University, East Lansing, MI 48824, USA.

⁴ Department of Electrical and Computer Engineering,

Michigan State University, East Lansing, MI 48824, USA.

November 18, 2025

Abstract

Single-cell data analysis seeks to characterize cellular heterogeneity based on high-dimensional gene expression profiles. Conventional approaches represent each cell as a vector in Euclidean space, which limits their ability to capture intrinsic correlations and multiscale geometric structures. We propose a multiscale framework based on Grassmann manifolds that integrates machine learning with subspace geometry for single-cell data analysis. By generating embeddings under multiple representation scales, the framework combines their features from different geometric views into a unified Grassmann manifold. A power-based scale sampling function is introduced to control the selection of scales and balance information across resolutions. Experiments on nine benchmark single-cell RNA-seq datasets demonstrate that the proposed approach effectively preserves meaningful structures and provides stable clustering performance, particularly for small to medium-sized datasets. These results suggest that Grassmann manifolds offer a coherent and informative foundation for analyzing single cell data.

Keywords: Grassmann manifolds, multiscale, subspace representation, single-cell data analysis

1 Introduction

Single-cell sequencing has become an important tool for studying cellular heterogeneity and elucidating biological mechanisms at the single-cell level [11]. Modern single-cell sequencing technologies measure the expression levels of tens of thousands of genes across tens of thousands of cells, producing data with extremely high dimensionality and complex nonlinear structure. To analyze such data effectively, it is essential to employ mathematical representations that preserve geometric structure while capturing biologically meaningful variation.

*Corresponding author. Email: weig@msu.edu

Despite these advances, many widely used analytical approaches, including principal component analysis (PCA) [7], t-distributed stochastic neighbor embedding (t-SNE) [31], and non-negative matrix factorization (NMF) [26], still represent each cell as a relatively high-dimensional vector in Euclidean space and perform dimension reduction or clustering based on Euclidean similarity. Although these Euclidean formulations are easy to implement, they cannot fully capture the correlations and structured relationships among cells that define the organization of high-dimensional single-cell populations.

Graph-based deep learning models, such as graph neural networks (GNNs) [28], attempt to address this limitation by constructing cell-cell graphs and propagating information through message passing, yet their representations remain in Euclidean space and thus fail to describe the intrinsic non-Euclidean geometry of single-cell manifolds.

Many single-cell analysis methods also rely on scale-related parameters that determine the resolution with which structural patterns are captured. Different scales reveal distinct biological or geometric characteristics: smaller scales emphasize local cellular transitions and fine-grained variability, whereas larger scales capture global organization, lineage relationships, and inter-cluster structure. For instance, methods such as UMAP, t-SNE, and topological PCA adjust the size to control the level of detail in their embeddings.

In recent years, the development of topological and geometric methods for single-cell analysis has received increasing attention [36, 39]. These approaches aim to model the intrinsic structure and dynamics of cellular populations through mathematically grounded principles, offering more interpretable and theoretically consistent analyses compared to purely empirical algorithms [35]. For example, the Hodge decomposition of single-cell RNA velocity [37] applies discrete exterior calculus to decompose cellular flow fields into curl-free, divergence-free, and harmonic components, providing a topologically interpretable description of cell-state transitions. Similarly, the topological principal component analysis (tPCA) framework [13] integrates persistent Laplacian operators with spectral regularization to capture multiscale geometric relationships in transcriptomic manifolds. From a topological perspective, scGeom [22] leverages curvature and persistent homology to reveal higher-order geometric organization among cells, while topological nonnegative matrix factorization (tNMF) [20] extends classical NMF by incorporating persistent homology for topologically informed feature extraction. In addition, the geometric structure-guided NMF model [10] combines matrix factorization with manifold regularization to improve the geometric interpretability of gene deconvolution. Together, these works highlight the growing importance of topological and geometric representations as mathematical tools for uncovering the complex organization of single-cell systems.

Other mathematical frameworks, including multiscale clustering approaches (MCIST) [14] and optimal transport [8] were proposed for spatial transcriptomic data analysis. Both MCIST and graph neural networks [28] achieve similar effects by varying the connectivity or depth in the underlying graph. Even in CCP-based methods, the number of gene clusters can be tuned to obtain multiscale features that reflect different biological resolutions. Recent multiscale and multi-fusion frameworks, such as the single-cell multiscale clustering framework (scMSCF) [23] and multi-fusion graph neural network (scMFGNN) [43], attempt to integrate information from different scales or omics layers. However, such concatenation-based strategies often treat multi-view features as independent and ignore their geometric relationships, limiting their ability to represent the hierarchical and correlated structures of single-cell data. These observations suggest that developing new representations of single-cell data in non-Euclidean spaces is a promising direction for capturing multiscale and multi-view biological information more effectively.

Grassmann manifolds provide a natural and general mathematical framework for representing structured and correlated data. Unlike Euclidean representations that treat each feature as an independent coordinate, Grassmann manifolds represent data as linear subspaces that inherently capture correlations and shared structures among multiple views. Formally, the Grassmann manifold, denoted as $\mathbf{Gr}(p, n)$, is the set of all p -dimensional linear subspaces of \mathbb{R}^n , where each subspace corresponds to a single point on the manifold. This subspace-based formulation provides a coherent geometric representation for data exhibiting structured

dependencies [25]. Grassmann manifolds have been successfully applied in computer vision and pattern recognition [9], where subspace representations capture intrinsic variations such as pose, illumination, or temporal dynamics. More recently, Li et al. [29] have extended Grassmann manifold geometry to the biological domain by representing genome sequences as points on a Grassmann manifold derived from frequency chaos game representations (FCGRs), providing a geometric perspective for comparing genomic structures.

However, the application of Grassmann manifolds to single-cell data analysis remains largely unexplored. Unlike images or genomic sequences, there is no straightforward or biologically intuitive way to represent an individual cell as a subspace, which poses a challenge in adapting this framework to single-cell applications. Nevertheless, the ability of Grassmann manifolds to capture multi-view correlations and encode structured variability across scales makes them a compelling mathematical foundation for representing single-cell data. Results obtained at a single scale are often insufficient to capture the full structural complexity of single-cell data, as each scale provides only a partial view of the underlying manifold. To address this limitation, we propose a general framework based on the Grassmann manifold that aggregates representations obtained at multiple scales into a unified subspace. This design integrates complementary geometric information across scales, providing a more comprehensive and stable representation of single-cell data.

In this work, we propose a new multiscale Grassmann manifolds framework for representing single-cell data. Each cell is modeled as a point on the Grassmann manifold constructed from its multiscale embeddings. The framework introduces a scale sampling function that selects and combines scales to balance computational efficiency and information richness. Pairwise similarities between cells are then computed using Grassmann manifold metrics such as the geodesic or chordal distance, and clustering is performed directly within the Grassmann manifold. Through experiments on several benchmark single-cell RNA-seq datasets, we demonstrate that the proposed multiscale Grassmann manifolds framework produces stable embeddings, improves clustering performance, and provides a more coherent biological organization of cells.

The remainder of this paper is organized as follows. In Section 2, we present the mathematical foundations underlying this work, including the definitions of the Grassmann manifold, its geometric structures and distance metrics, and the concept of subspace representation. Section 3 then describes the proposed framework for representing single-cell data in the Grassmann manifold and explains how multiscale subspaces are constructed through a scale sampling function. Next, Section 4 presents experimental results on benchmark single-cell datasets and compares the performance of the proposed multiscale Grassmann manifolds framework with several existing methods. A detailed discussion of the framework is provided in Section 5, and the paper concludes with final remarks in Section 6.

The main contributions of this paper are summarized as follows:

1. We propose the multiscale Grassmann manifolds framework for representing single-cell data, which integrates embeddings from multiple scales into a unified subspace representation.
2. We design a power-based scale sampling function that adaptively selects sizes to balance local and global geometric information across scales.
3. The proposed framework is flexible and extendable, and can be combined with alternative dimensionality reduction methods capable of capturing multi-view information via the varying of scales.

2 Mathematical Foundations

This section presents the mathematical foundations of the proposed framework. We first introduce the definition and equivalent formulations of the Grassmann manifold, which provide the geometric setting for our model. Next, we describe its key geometric structures, including the tangent space, Riemannian metric, and geodesic formulation, followed by commonly used distance metrics that quantify similarities between

subspaces. Finally, we explain how data can be represented as subspaces on the Grassmann manifold, linking its geometry to multiscale data modeling. The main notation used throughout this paper is summarized in Table 1.

Symbol	Description
\mathbb{R}	Real number field
\mathbb{R}^n	n -dimensional real vector space
$\mathbb{R}^{n \times n}$	Set of all real $n \times n$ matrices
A^T	Transpose of matrix A
$\mathbf{Gr}(n, p)$	Grassmann manifold of all p -dimensional subspaces in \mathbb{R}^n
$\Theta(\mathcal{X}, \mathcal{Y})$	Principal angles between two subspaces \mathcal{X} and \mathcal{Y}
$\dim(\mathcal{U})$	Dimension of subspace \mathcal{U}
$\text{rank}(P)$	Rank of matrix P
$\text{span}(\cdot)$	Linear span of the given vectors
$T_P \mathbf{Gr}(n, p)$	Tangent space at $p \in \mathbf{Gr}(n, p)$
$O(p)$	Orthogonal group of order p
$\text{GL}(n)$	General linear group of order n
$\gamma(t)$	Geodesic curve on $\mathbf{Gr}(n, p)$ parameterized by t
$\dot{\gamma}(t)$	Tangent (velocity) vector of $\gamma(t)$ at parameter t
I_p	$p \times p$ identity matrix
$\text{Tr}(\cdot)$	Trace operator of a square matrix
$\exp(\cdot)$	Matrix exponential map
$\log(\cdot)$	Principal matrix logarithm
Φ	Subspace embedding map $\Phi : \mathcal{X} \mapsto P \in \mathbf{Gr}(n, p)$

Table 1: Notations used in this paper.

2.1 Definitions of the Grassmann Manifold

The Grassmann manifold can be characterized in several mathematically equivalent ways, each describing its elements as p -dimensional linear subspaces of \mathbb{R}^n [1, 3, 5]. Formally, each element of $\mathbf{Gr}(n, p)$ represents a p -dimensional linear subspace of \mathbb{R}^n , defined as

$$\mathbf{Gr}(n, p) = \{ \mathcal{U} \subset \mathbb{R}^n \mid \dim(\mathcal{U}) = p \}.$$

This provides an abstract geometric definition of the manifold as the collection of all p -dimensional subspaces. The Grassmann manifold admits several equivalent perspectives for describing its elements as p -dimensional subspaces of \mathbb{R}^n . These perspectives emphasize different aspects of the same geometric object and are often used interchangeably in both theoretical analysis and applications.

(1) Basis perspective. A subspace $\mathcal{U} \in \mathbf{Gr}(n, p)$ can be represented by any full-rank matrix $Y \in \mathbb{R}^{n \times p}$ whose columns form a basis of \mathcal{U} . Two matrices Y_1 and Y_2 define the same subspace if there exists a nonsingular matrix $R \in \text{GL}(p)$ such that $Y_1 = Y_2 R$, meaning that all matrices whose columns span the same subspace are equivalent under right multiplication by an invertible transformation. This perspective identifies $\mathbf{Gr}(n, p)$ with the equivalence class of all rank- p matrices whose column spaces coincide. (See, e.g., [1] for a general overview.)

(2) Orthonormal basis (ONB) perspective. Alternatively, each subspace can be described by a matrix

$U \in \mathbb{R}^{n \times p}$ whose columns form an orthonormal basis of \mathcal{U} , satisfying $U^\top U = I_p$. All matrices related by right multiplication with an orthogonal matrix $R \in O(p)$ represent the same subspace, i.e., UR and U correspond to the same point on $\mathbf{Gr}(n, p)$. This orthonormal form is particularly convenient for analysis involving differential geometry or optimization on manifolds [17].

(3) Projector perspective. Each subspace \mathcal{U} can also be uniquely characterized by its orthogonal projection operator $P : \mathbb{R}^n \rightarrow \mathbb{R}^n$ onto \mathcal{U} , given by

$$P = UU^\top,$$

where U is any orthonormal basis of \mathcal{U} . The collection of all such projectors forms an equivalent representation of the Grassmann manifold:

$$\mathbf{Gr}(n, p) = \{ P \in \mathbb{R}^{n \times n} \mid P^2 = P, P^\top = P, \text{rank}(P) = p \}.$$

This formulation embeds $\mathbf{Gr}(n, p)$ into the space of symmetric matrices and serves as a foundation for defining distances and inner products between subspaces [3].

While these perspectives differ in representation, they describe the same geometric structure of the Grassmann manifold. Each viewpoint serves different computational purposes: the basis form emphasizes linear independence, the ONB form ensures orthogonality and numerical stability, and the projector form conveniently expresses geometric relations between subspaces.

2.2 Geometric Structure and Distance Metrics

In this section, we review key geometric structures of the Grassmann manifold based on its projector representation, which is particularly suitable for expressing its differential and Riemannian properties in matrix form

$$\mathbf{Gr}(n, p) = \{ P \in \mathbb{R}^{n \times n} \mid P^2 = P, P^\top = P, \text{rank}(P) = p \}.$$

Each point P represents an orthogonal projector onto a p -dimensional subspace of \mathbb{R}^n . This formulation is particularly convenient for expressing differential and geometric properties in matrix form.

Tangent space. At a point $P \in \mathbf{Gr}(n, p)$, the tangent space is given by

$$T_P \mathbf{Gr}(n, p) = \{ [\Omega, P] = \Omega P - P \Omega \mid \Omega^\top = -\Omega \}, \quad (1)$$

where Ω belongs to the set of skew-Hermitian matrices. Equivalently, every tangent vector $\Delta \in T_P \mathbf{Gr}(n, p)$ can be written in block form

$$\Delta = Q \begin{bmatrix} 0 & B^\top \\ B & 0 \end{bmatrix} Q^\top, \quad B \in \mathbb{R}^{(n-p) \times p}, Q \in O(n).$$

The canonical Riemannian metric on $\mathbf{Gr}(n, p)$ is induced from the ambient Euclidean space of matrices. For two tangent vectors $\Delta_1 = [\Omega_1, P]$ and $\Delta_2 = [\Omega_2, P]$, their inner product is defined by

$$\langle \Delta_1, \Delta_2 \rangle_P = \frac{1}{2} \text{Tr}(\Delta_1^\top \Delta_2) = \text{Tr}(\Omega_1^\top \Omega_2), \quad (2)$$

where $\text{Tr}(\cdot)$ denotes the matrix trace. This metric is invariant under the orthogonal group action $P \mapsto QPQ^\top$ for any $Q \in O(n)$, ensuring that it depends only on the subspaces, not on the particular matrix representation. It provides the geometric foundation for defining geodesics and curvature on $\mathbf{Gr}(n, p)$.

Geodesic. With the canonical metric in (2), the Grassmann manifold $\mathbf{Gr}(n, p)$ admits a smooth geodesic flow generated by the matrix exponential. For a point $P \in \mathbf{Gr}(n, p)$ and a tangent direction $\Delta = [\Omega, P] \in T_P \mathbf{Gr}(n, p)$, the geodesic $\gamma(t)$ starting at P with initial velocity Δ is given by [5]

$$\gamma(t) = \exp(t\Omega) P \exp(-t\Omega), \quad (3)$$

where $\exp(\cdot)$ denotes the matrix exponential map, and the curve satisfies

$$\gamma(0) = P, \quad \dot{\gamma}(0) = \Delta.$$

When the matrix $(I - 2Q)(I - 2P)$ has no negative real eigenvalues, the minimizing geodesic between two points $P, Q \in \mathbf{Gr}(n, p)$ admits the following closed-form expression [3]:

$$\gamma(t) = e^{\frac{t}{2} \log((I-2Q)(I-2P))} P e^{-\frac{t}{2} \log((I-2Q)(I-2P))}, \quad t \in [0, 1], \quad (4)$$

where \log denotes the principal matrix logarithm. Equation (4) describes the shortest geodesic from P to Q under the canonical metric whenever such a unique minimizing path exists.

Distance Metrics. The shortest path between two points on $\mathbf{Gr}(n, p)$, defined by the geodesic above, can be equivalently characterized in terms of the relative orientation between subspaces, quantified by a set of principal angles.

Definition 2.1 (Principal Angles). Let $\mathcal{X}, \mathcal{Y} \subset \mathbb{R}^n$ be two subspaces with $\dim(\mathcal{X}) = p$ and $\dim(\mathcal{Y}) = q$, and let $m = \min(p, q)$. The principal angles between \mathcal{X} and \mathcal{Y} are defined as

$$\Theta(\mathcal{X}, \mathcal{Y}) = [\theta_1, \dots, \theta_m], \quad \theta_i \in [0, \frac{\pi}{2}], \quad i = 1, \dots, m,$$

where $\cos(\theta_i)$ are the singular values of $U_{\mathcal{X}}^{\top} U_{\mathcal{Y}}$, and $U_{\mathcal{X}}, U_{\mathcal{Y}}$ are orthonormal basis matrices for \mathcal{X} and \mathcal{Y} , respectively. The corresponding vectors $\{x_i\}$ and $\{y_i\}$ that achieve these angles are called the principal vectors.

The principal angles provide a direct way to quantify the smallest angular deviations between subspaces and form the basis for defining various distance measures on $\mathbf{Gr}(n, p)$. Different distance functions have been proposed in the literature, which can be equivalently expressed using either principal angles or orthonormal basis representations [45]. Several representative metrics are summarized in Table 2.

Table 2: Common distance metrics on $\mathbf{Gr}(n, p)$ expressed in terms of principal angles $\{\theta_i\}_{i=1}^p$ between \mathcal{X} and \mathcal{Y} .

Metric	Notation	Definition (principal-angle form)
Geodesic	$d_{\text{geo}}(\mathcal{X}, \mathcal{Y})$	$\left(\sum_{i=1}^p \theta_i^2 \right)^{1/2}$
Chordal	$d_{\text{chord}}(\mathcal{X}, \mathcal{Y})$	$\left(\sum_{i=1}^p \sin^2 \theta_i \right)^{1/2}$
Fubini–Study	$d_{\text{FS}}(\mathcal{X}, \mathcal{Y})$	$\cos^{-1} \left(\prod_{i=1}^p \cos \theta_i \right)$
Martin	$d_{\text{Martin}}(\mathcal{X}, \mathcal{Y})$	$\left(\log \prod_{i=1}^p \frac{1}{\cos^2 \theta_i} \right)^{1/2}$
Procrustes	$d_{\text{Proc}}(\mathcal{X}, \mathcal{Y})$	$2 \left(\sum_{i=1}^p \sin^2 \left(\frac{\theta_i}{2} \right) \right)^{1/2}$

2.3 Subspace Representation

In Euclidean models, each data instance is represented by a single vector $x_i \in \mathbb{R}^n$, and similarity is typically measured using Euclidean or correlation-based distances. Such point-wise representations, however, neglect internal structure, correlations, and multi-view variability that may exist within a sample or across multiple observations. A more general and geometrically consistent approach is to represent each instance by a low-dimensional subspace, which lies on the Grassmann manifold $\mathbf{Gr}(n, p)$.

Definition 2.2 (Subspace Representation). Let $\mathfrak{X} = \{x_1, x_2, \dots, x_m\} \subset \mathbb{R}^n$ be a set of feature vectors associated with a single object, cell, or sample measured under different conditions. A *subspace representation* of \mathfrak{X} is defined as the linear subspace

$$\mathcal{S} = \text{span}(Y), \quad Y = [x_1, x_2, \dots, x_p] \in \mathbb{R}^{n \times p}, \text{rank}(Y) = p.$$

After orthonormalization, the basis matrix \tilde{Y} satisfies $\tilde{Y}^\top \tilde{Y} = I_p$, and the subspace \mathcal{S} corresponds to a point on the Grassmann manifold $\mathbf{Gr}(n, p)$.

Equivalently, a subspace can be represented by its orthogonal projection matrix

$$P = \tilde{Y} \tilde{Y}^\top, \quad P^\top = P, P^2 = P, \text{rank}(P) = p,$$

which uniquely characterizes \mathcal{S} and enables the use of distance metrics in Table 2 for comparing different samples. The mapping

$$\Phi : \mathfrak{X} \mapsto P \in \mathbf{Gr}(n, p)$$

is referred to as the *subspace embedding map*, which projects a collection of feature vectors into the space of p -dimensional subspaces.

Subspace representations possess several useful mathematical properties. They are invariant under orthogonal transformations of the basis, i.e., $\text{span}(Y) = \text{span}(YR)$ for any $R \in O(p)$, and they encode higher-order correlations among the columns of Y , providing a compact description of structured or multi-view data. When distances between subspaces are measured using metrics on $\mathbf{Gr}(n, p)$, the resulting geometry captures relationships that are robust to noise, rotation, and small perturbations in the original feature space.

3 Multiscale Representation of Single-Cell Data on the Grassmann Manifold

This section introduces the proposed multiscale Grassmann manifolds (MGM) framework, which provides a unified geometric representation of single-cell data by integrating information obtained from multiple scales. We first present the overall procedure for representing single-cell data as points on the Grassmann manifold through embeddings constructed under multiple representation scales. An overview of the workflow is illustrated in Figure 1. Next, we describe a scale sampling function that determines the set of scales used to generate multiscale embeddings. Finally, the resulting Grassmann manifold representations yield a distance matrix that can be directly applied to downstream analyses, including clustering or classification, by replacing Euclidean metrics with Grassmann manifold distances.

3.1 Framework Overview of Multiscale Grassmann Manifolds Framework for Single-Cell Representation

Given a single-cell expression matrix

$$X = \begin{pmatrix} x_1 \\ x_2 \\ \vdots \\ x_M \end{pmatrix} \in \mathbb{R}^{M \times N},$$

where M denotes the number of cells, N denotes the number of genes, and each row vector $x_j \in \mathbb{R}^{1 \times N}$ represents the gene expression profile of cell j for $j = 1, 2, \dots, M$, the goal of the framework is to construct a Grassmann manifold-based representation that captures the intrinsic structure of the dataset across multiple scales.

Stage 1: Multiscale embeddings. The first step of the multiscale Grassmann manifolds framework is to generate low-dimensional representations that capture cellular features under multiple or resolution scales. Let p denote the number of scales considered in the multiscale setting, that is, the total number of embeddings generated under different scale parameters. Each scale produces an embedding of dimension n , which represents the number of features preserved for each cell after applying a suitable dimension reduction method. The set of scales is defined as

$$S = \{s_1, s_2, \dots, s_p\},$$

where each s_i is determined by a sampling function f_{sample} , which will be introduced in Section 3.2. For all scales, the embedding dimension n is fixed to ensure consistency across representations. Applying the selected dimension reduction method under the scales s_1, s_2, \dots, s_p yields a sequence of feature matrices

$$E_i = \begin{pmatrix} z_1^{(i)} \\ z_2^{(i)} \\ \vdots \\ z_M^{(i)} \end{pmatrix} = \text{MDR}(X; s_i) \in \mathbb{R}^{M \times n}, \quad i = 1, 2, \dots, p,$$

where $\text{MDR}(X; s_i)$ denotes a multiscale dimension reduction (MDR) operation applied to the single-cell dataset X under scale parameter s_i . Each row vector $z_j^{(i)} \in \mathbb{R}^{1 \times n}$ represents the embedding of cell j at scale s_i . Each matrix E_i therefore contains the n -dimensional embeddings of all M cells under the corresponding scale. These multiscale embeddings provide complementary geometric views of the dataset, where smaller scales emphasize fine-grained local transitions, while larger scales capture broader global organization across the cellular manifold.

Stage 2: Feature aggregation. For each cell $j = 1, 2, \dots, M$, we collect its feature vectors obtained from all p embeddings generated under different scales. These multiscale features are concatenated column-wise to form a matrix

$$Z_j = \begin{bmatrix} (z_j^{(1)})^\top & (z_j^{(2)})^\top & \dots & (z_j^{(p)})^\top \end{bmatrix} \in \mathbb{R}^{n \times p},$$

where $z_j^{(i)} \in \mathbb{R}^{1 \times n}$ denotes the embedding vector of cell j obtained at scale s_i . The matrix Z_j integrates multiple geometric views of the same cell across different scales, thereby capturing complementary information that would otherwise be lost in a single-scale representation.

Stage 3: Grassmann manifold representation. After assembling the multiscale feature matrix Z_j for each cell, we interpret its column space as a subspace in \mathbb{R}^n . Formally, the span of the feature vectors across all scales defines

$$G_j = \text{span}(Z_j) = \text{span}\{ (z_j^{(1)})^\top, (z_j^{(2)})^\top, \dots, (z_j^{(p)})^\top \} \in \mathbf{Gr}(n, p),$$

where each $z_j^{(i)}$ corresponds to the embedding of cell j obtained at scale s_i . The resulting subspace G_j characterizes cell j in a multiscale feature space, and all cells are thus represented as points on the Grassmann Manifold $\mathbf{Gr}(n, p)$.

Stage 4: Distance computation on the Grassmann manifold. Based on the subspace representation $\{G_j\}_{j=1}^M$, we compute pairwise distances between all cells using the Grassmann manifold metrics introduced in Section 2. Commonly used distance measures include the geodesic distance and the chordal distance, both of which quantify the geometric discrepancy between two subspaces in $\mathbf{Gr}(n, p)$. For each pair of cells (i, j) , the Grassmann manifold distance $d(G_i, G_j)$ is computed according to the selected metric in Table 2, forming a symmetric distance matrix

$$D = [d_{ij}]_{i,j=1}^M = [d(G_i, G_j)]_{i,j=1}^M \in \mathbb{R}^{M \times M}.$$

This distance matrix serves as the foundation for downstream analyses, such as clustering, visualization, or classification, by providing a non-Euclidean measure of similarity that reflects the multiscale geometric relationships between cells.

Algorithm 1 summarizes the complete multiscale Grassmann manifolds (MGM) representation procedure, and the overall workflow is illustrated in Figure 1.

```

1: Input: Single-cell data matrix  $X \in \mathbb{R}^{M \times N}$ ; scale set  $S = \{s_1, s_2, \dots, s_p\}$ ; embedding dimension  $n$ 
2: Output: Cell representations  $\{G_j\}_{j=1}^M \subset \mathbf{Gr}(n, p)$  and pairwise distance matrix  $D \in \mathbb{R}^{M \times M}$ 
Stage 1: Multiscale dimension reduction
3: for  $i = 1$  to  $p$  do
4:    $E_i \leftarrow \text{MDR}(X; s_i) \in \mathbb{R}^{M \times n}$   $\triangleright E_i = [z_1^{(i)}; z_2^{(i)}; \dots; z_M^{(i)}]$ 
5: end for
Stage 2: Feature aggregation
6: for  $j = 1$  to  $M$  do
7:    $Z_j \leftarrow [(z_j^{(1)})^\top, (z_j^{(2)})^\top, \dots, (z_j^{(p)})^\top] \in \mathbb{R}^{n \times p}$   $\triangleright$  multiscale feature matrix for cell  $j$ 
8: end for
Stage 3: Grassmann manifold representation
9: for  $j = 1$  to  $M$  do
10:   $G_j \leftarrow \text{span}(Z_j)$   $\triangleright$  interpret each  $Z_j$  as a  $p$ -dimensional subspace on  $\mathbf{Gr}(n, p)$ 
11: end for
Stage 4: Distance computation
12: Compute pairwise distances  $d_{jk} \leftarrow d_{\mathbf{Gr}}(G_j, G_k)$  using Grassmann Manifold metrics (e.g., geodesic or chordal distance).
13: return  $\{G_j\}_{j=1}^M, D$ 

```

Algorithm 1: Multiscale Grassmann Manifolds (MGM)

3.2 Sampling Function for Multiscale Selection

To generate the scales used by the framework, we adopt a power-based sampling function that flexibly controls the density of sampled scales across a prescribed interval. Given a minimum and maximum size $a = s_{\min}$ and $b = s_{\max}$, a target number of samples $n_{\text{scales}} \geq 2$, and a fixed exponent $p_s > 0$, we first compute raw (real-valued) samples

$$\tilde{s}_i = a + (b - a) t_i^{p_s}, \quad t_i = \frac{i}{n_{\text{scales}} - 1}, \quad i = 0, 1, \dots, n_{\text{scales}} - 1. \quad (5)$$

We then quantize $\{\tilde{s}_i\}$ to integer sizes and remove duplicates to obtain the final, ordered scale set

$$S = \{s_1 < s_2 < \dots < s_p\} \subset \{a, a + 1, \dots, b\}.$$

Here $p = |S|$ is the number of distinct scales returned by the sampling function, which may satisfy $p \leq n_{\text{scales}}$ due to quantization and de-duplication. Throughout the framework, p also determines the number of multiscale views per cell and hence the rank on $\mathbf{Gr}(n, p)$. To avoid notational conflict, p_s denotes the sampling exponent and should not be confused with p . In practice we typically choose $p_s > 1$ (e.g., $p_s = 1.6$) to bias the sampling toward smaller s (denser local views) while still covering the full range $[a, b]$. Algorithm 2 implements the power-based sampling f_{sample} .

Remark 3.1. *The exponent p_s in the power-based sampling function controls the density of sampled scales across the range $[a, b]$. When $p_s = 1$, the sampling is linear, producing uniformly spaced scales. For $p_s < 1$, more scales are concentrated toward the larger sizes (favoring global structure), whereas for $p_s > 1$, the sampling becomes denser near smaller s (emphasizing local information). In our experiments, for datasets*

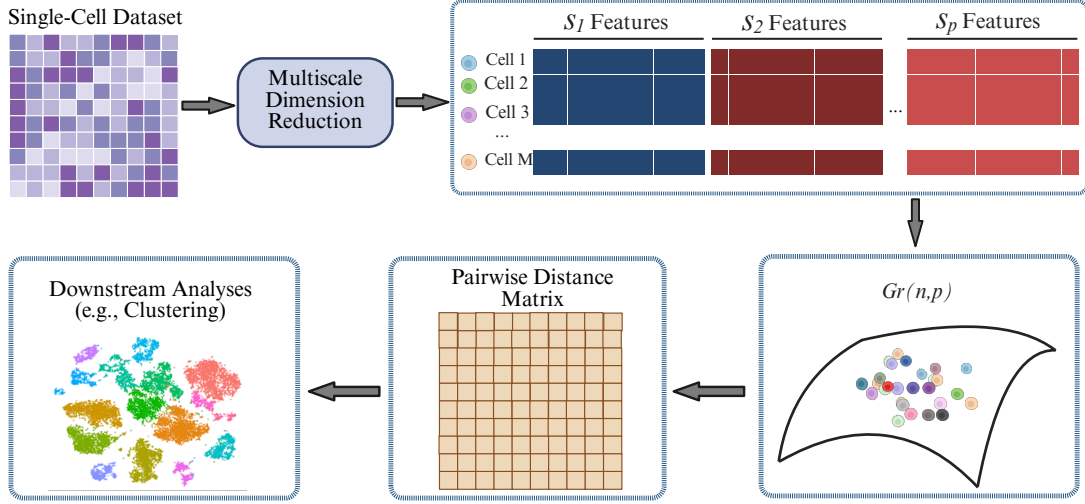


Figure 1: Overview of the proposed multiscale Grassmann manifolds (MGM) framework. Starting from a single-cell gene expression matrix, multiple low-dimensional embeddings are generated under different neighborhood sizes (s_1, \dots, s_p) using a chosen dimensionality reduction method. For each cell, the resulting multiscale feature vectors are aggregated into a matrix whose column space defines a subspace on the Grassmann manifold $\mathbf{Gr}(n, p)$. Pairwise distances between these subspaces are then computed to form a pairwise distance matrix, which can be used for downstream analyses such as clustering.

-
- 1: **Input:** bounds $a, b \in \mathbb{N}$ with $2 \leq a < b$; number of samples $n_{\text{scales}} \geq 2$; exponent $p_s > 0$
 - 2: **Output:** ordered, unique scales $S = \{s_1, \dots, s_p\}$ with $a \leq s_1 < \dots < s_p \leq b$
 - 3: Generate $t_i \leftarrow i / (n_{\text{scales}} - 1)$ for $i = 0, 1, \dots, n_{\text{scales}} - 1$
 - 4: Compute raw values $\tilde{s}_i \leftarrow a + (b - a) t_i^{p_s}$
 - 5: Quantize $q_i \leftarrow \text{round}(\tilde{s}_i)$ and clip: $q_i \leftarrow \min\{\max\{q_i, a\}, b\}$
 - 6: Form $S \leftarrow$ the sorted set of unique values in $\{q_i\}_{i=0}^{n_{\text{scales}}-1}$ \triangleright now $p = |S| \leq n_{\text{scales}}$
 - 7: **return** $S = \{s_1, \dots, s_p\}$
-

Algorithm 2: Power-based sampling function $f_{\text{sample}}(a, b, n_{\text{scales}}, p_s)$

with a relatively small number of cells (for datasets with fewer than or around 1000 cells), we set $a = 5$, $b = n$, and use $p_s = 1.6 > 1$ to obtain finer resolution among smaller-scale s while maintaining coverage of the full range.

3.3 Clustering and Performance Evaluation

Once each cell is represented as a point on the Grassmann manifold $\mathbf{Gr}(n, p)$, the resulting pairwise distance matrix provides a flexible foundation for various downstream analyses. Standard clustering or classification algorithms can be readily extended by substituting the Euclidean distance with a Grassmann manifold metric. This allows clustering to be performed directly in the manifold space, where the subspace geometry captures intrinsic relationships among samples more effectively than Euclidean representations.

A number of clustering and recognition methods based on the Grassmann manifold geometry have been proposed in related fields. One of the earliest examples is the Grassmann Nearest Neighbor (GNN) algorithm introduced by Yamaguchi et al. [42], which classifies each point on the manifold by comparing its geodesic distance to the nearest class subspace. Subsequent studies extended this concept to unsupervised settings, including k -means clustering on Grassmann manifolds [27] and spectral clustering based on Grassmann manifold affinity matrices [24, 44]. These methods leverage the manifold’s intrinsic geometry to improve robustness to noise and nonlinear variation.

To evaluate clustering performance, we employ five commonly used metrics in single-cell analysis: clustering accuracy (ACC) [15], normalized mutual information (NMI) [41], adjusted Rand index (ARI) [21], purity [34], and average purity (Avg-Purity) [38]. The definitions of these metrics are provided in the Supporting Information. Each metric compares the predicted cluster labels with the ground-truth cell labels, offering complementary perspectives on clustering accuracy, label consistency, and partition quality. Detailed results and comparisons with baseline methods are presented in Section 4.

4 Experiments

This section presents the experimental evaluation of the proposed multiscale Grassmann manifolds (MGM) framework and its performance on benchmark single-cell RNA-seq datasets. We aim to examine how the manifold-based representation improves single-cell data analysis by comparing its clustering performance with standard Euclidean and manifold-based approaches. All experiments were conducted on publicly available benchmark datasets, and comparative analyses were performed under consistent preprocessing and clustering conditions.

4.1 Datasets and Experimental Setup

The proposed framework was evaluated on nine publicly available human single-cell RNA-seq datasets that span a range of sizes—from small datasets with fewer than 50 cells to large datasets with nearly 2,000 cells. These datasets have been widely used in previous studies (e.g., [18, 20]) and are considered reliable benchmarks for evaluating dimensionality reduction and clustering performance.

Table 3 summarizes the main characteristics of the datasets, including the number of cells and genes. This collection provides a balanced test bed for evaluating the method across different data scales.

Table 3: Summary of benchmark single-cell RNA-seq datasets used in the experiments. Each dataset includes its GEO accession number, reference, number of annotated cell types, and the numbers of samples (cells) and genes.

GEO accession	Reference	Cell types	Samples	Genes
GSE75748time	Chu [12]	6	758	19 189
GSE94820	Villani [40]	5	1 140	26 593
GSE67835	Dramanis [16]	8	420	22 084
GSE75748cell	Chu [12]	6	1 018	19 189
GSE109979	Lu [30]	4	329	18 840
GSE84133human1	Baron [2]	9	1 895	20 125
GSE84133human2	Baron [2]	9	1 702	20 125
GSE84133human4	Baron [2]	6	1 275	20 125
GSE57249	Biase [6]	3	49	25 737

For each dataset, gene expression matrices were normalized and log-transformed according to standard preprocessing procedures. To systematically evaluate the performance of the proposed framework, we designed two experimental configurations that differ in preprocessing rigor and noise levels. The first setup (noisy condition) tests the robustness of the model under high-noise data, while the second setup (refined condition) focuses on well-preprocessed data to examine representational quality in cleaner manifolds. In both settings, the proposed method was compared with widely used dimensionality reduction and clustering baselines.

In the noisy setting, the proposed method was compared with Avg-UMAP (obtained by averaging the embeddings across all scales) and PCA. In the refined setting, results for Nonnegative Matrix Factorization

(NMF) and t-SNE were directly adopted from previous studies [18,20] for baseline comparison. Both methods were evaluated using k-means as the downstream algorithm, ensuring consistency with our experimental setup.

Setup I: Noisy condition. In this configuration, single-cell expression matrices were first reduced to 200 dimensions by PCA and then embedded into a 100-dimensional space using a multiscale dimensionality reduction process. Neighborhood scales were generated by the power-based sampling function with exponent $p_s = 2$. For most datasets, the number of sampled scales was set to $n_{\text{scales}} = 25$, yielding a subspace rank of $p = 23$ and a Grassmann representation in $\mathbf{Gr}(100, 23)$. For the smallest dataset, GSE57249, which contains only 49 cells, we used $n_{\text{scales}} = 13$ and $p = 12$ to maintain computational stability. This setup evaluates the robustness of the proposed framework under conditions where residual background noise remains after preprocessing. Nine single-cell RNA-seq datasets were tested: GSE75748time, GSE94820, GSE67835, GSE75748cell, GSE109979, GSE84133human1, GSE84133human2, GSE84133human4, and GSE57249. The method was compared with Avg-UMAP and PCA under identical settings to assess its ability to preserve geometric consistency in noisy embeddings.

Setup II: Refined condition. In this configuration, single-cell data were carefully preprocessed to reduce background noise and retain the most informative features. For small to medium datasets, including GSE75748time, GSE94820, GSE67835, GSE75748cell, and GSE109979, the gene expression matrices were reduced to 50 dimensions by PCA and further embedded to $n = 20$ dimensions. Each cell was then represented by a subspace of rank $p = 10$, forming points on the Grassmann manifold $\mathbf{Gr}(20, 10)$. For larger datasets, including GSE84133human1, GSE84133human2, and GSE84133human4, PCA reduction to 100 dimensions and embedding to $n = 50$ were used, with a subspace rank of $p = 19$, corresponding to $\mathbf{Gr}(50, 19)$. For the smallest dataset, GSE57249, PCA and embedding dimensions were set to 20 and 15, respectively, with a subspace rank of $p = 8$ on $\mathbf{Gr}(15, 8)$. This refined configuration evaluates the representational power of the proposed framework when the data manifold is well preserved through preprocessing and the impact of noise is minimized.

Both setups employed the power-based sampling strategy introduced in Section 3.2 to generate scales, with different exponents reflecting their respective scale ranges. For Setup I, which uses a broader range ($[5, 100]$), the power exponent was set to $p_s = 2.0$ to achieve denser sampling at smaller sizes. For Setup II, where the scale interval is narrower, $p_s = 1.6$ was used instead. In all experiments, the chordal distance was adopted for Grassmann manifold affinity computation. All models were implemented in Python and evaluated under the same computational environment to ensure fair and reproducible comparison. The full parameter configurations for Setup I and Setup II are provided in Section 1 of the Supporting Information.

Remark. The number of usable scales p is determined by the sampling function f_{sample} , which may produce redundant sizes after quantization. In practice, p denotes the number of unique scales obtained after removing duplicates from the generated set.

In the implementation, multiscale low-dimensional embeddings were generated through a multiscale dimension reduction process, where UMAP [4] was employed as the underlying dimensionality reduction method. These embeddings were then integrated using the proposed multiscale Grassmann manifolds (MGM) framework to form Grassmann manifold representations. Pairwise distances between cells were computed on the manifold using the chordal distance. For the noisy condition (Setup I), spectral clustering [33] was used as the downstream algorithm, while for the refined condition (Setup II), k -means clustering [32] was adopted to ensure consistency with the baseline methods reported in previous studies. The implementation details of UMAP, as well as the clustering settings including the specific configurations for spectral clustering and k -means, are provided in the Supporting Information. Unless otherwise specified, the chordal distance was employed as the default Grassmann metric. Visualization results were also provided to illustrate the behavior of the framework across multiple scales.

4.2 Results

This subsection presents the quantitative results of the proposed multiscale Grassmann manifolds (MGM) framework under the two experimental configurations described in Section 4.1. All methods were evaluated using five random seeds (1, 3, 5, 7, 9), and the reported values correspond to the averages across these runs. Clustering performance was assessed using standard evaluation metrics: accuracy (ACC), normalized mutual information (NMI), adjusted Rand index (ARI), purity, and average purity (Avg-Purity). For each dataset, the best-performing results are indicated in **bold**.

4.2.1 Results under the noisy condition (Setup I)

Under the noisy setting, the proposed multiscale Grassmann manifolds (MGM) framework was evaluated using spectral clustering and compared with PCA and Avg-UMAP. Despite the presence of residual noise after preprocessing, MGM achieved superior or comparable clustering results across most datasets. Quantitative results for clustering accuracy (ACC), normalized mutual information (NMI), adjusted Rand index (ARI), and purity are summarized in Tables 4–7.

Table 4: ACC under the noisy condition (Setup I). Best in **bold**.

Dataset	MGM	Avg-UMAP	PCA
GSE75748time	0.7219	0.6599	0.4222
GSE94820	0.7314	0.7391	0.6496
GSE67835	0.6819	0.4970	0.5581
GSE75748cell	0.8316	0.7568	0.3984
GSE109979	0.7732	0.7009	0.3463
GSE84133human1	0.6920	0.6599	0.5714
GSE84133human2	0.7053	0.5972	0.4401
GSE84133human4	0.7677	0.7323	0.5307
GSE57249	0.9102	0.8507	0.5388
Average ACC	0.7573	0.6882	0.4950

Table 5: NMI under the noisy condition (Setup I). Best in **bold**.

Dataset	MGM	Avg-UMAP	PCA
GSE75748time	0.6508	0.6005	0.2831
GSE94820	0.6721	0.6472	0.4916
GSE67835	0.6044	0.4520	0.4218
GSE75748cell	0.8164	0.7750	0.4220
GSE109979	0.5590	0.4939	0.1319
GSE84133human1	0.7382	0.7223	0.4677
GSE84133human2	0.7399	0.6364	0.3673
GSE84133human4	0.7571	0.7043	0.4010
GSE57249	0.7249	0.6589	0.2589
Average NMI	0.6959	0.6323	0.3606

To better illustrate the overall trends across all datasets, Figure 2 presents the average values of the four metrics, providing an intuitive comparison of the three methods under the noisy setup.

Analysis. Figure 2 summarizes the average performance of the compared methods across all nine benchmark datasets. The proposed multiscale Grassmann manifolds (MGM) framework consistently ranks first or second

Table 6: ARI under the noisy condition (Setup I). Best in **bold**.

Dataset	MGM	Avg-UMAP	PCA
GSE75748time	0.5238	0.4795	0.1620
GSE94820	0.5876	0.5546	0.3934
GSE67835	0.4904	0.2889	0.2657
GSE75748cell	0.6999	0.6451	0.2028
GSE109979	0.5189	0.4518	0.0495
GSE84133human1	0.5515	0.5084	0.2982
GSE84133human2	0.5871	0.4545	0.2235
GSE84133human4	0.6749	0.4570	0.2651
GSE57249	0.7293	0.6449	0.0839
Average ARI	0.5959	0.4983	0.2160

Table 7: Purity under the noisy condition (Setup I). Best in **bold**.

Dataset	MGM	Avg-UMAP	PCA
GSE75748time	0.7219	0.6946	0.4844
GSE94820	0.7693	0.7556	0.6672
GSE67835	0.7629	0.6275	0.6314
GSE75748cell	0.8316	0.7908	0.5477
GSE109979	0.7732	0.7049	0.3963
GSE84133human1	0.8434	0.8524	0.7404
GSE84133human2	0.9235	0.8285	0.6741
GSE84133human4	0.8933	0.8441	0.6504
GSE57249	0.9102	0.8592	0.5918
Average Purity	0.8255	0.7731	0.5982

across all four evaluation metrics, demonstrating greater stability than both Avg-UMAP and PCA under noisy conditions. MGM achieves the best performance on most datasets and maintains reliable results across all metrics, whereas PCA often shows substantial degradation in the presence of noise and Avg-UMAP exhibits higher variability across datasets. For medium-sized datasets such as GSE75748cell and GSE67835, the performance gap between MGM and the baselines is particularly pronounced, suggesting that the manifold-based representation more effectively preserves global and local structure when noise perturbs neighborhood geometry. Although Avg-UMAP slightly outperforms MGM in a few isolated cases (e.g., GSE94820 for ACC and GSE84133human1 for Purity), MGM provides the most balanced and consistent performance overall. Notably, on the smallest dataset, GSE57249, MGM attains the highest scores across all metrics, demonstrating strong robustness even under extreme sample sparsity. These findings confirm that aggregating multiscale information within a Grassmann manifold subspace yields a more noise-resilient and geometrically stable representation than single-scale embeddings.

4.2.2 Results under the refined condition (Setup II)

Under the refined setting, five methods were compared: PCA, NMF, rNMF, Avg-UMAP, and the proposed multiscale Grassmann manifolds (MGM) framework. With more rigorous preprocessing that reduces background noise and enhances data structure, MGM achieved the highest or comparable scores across most datasets and evaluation metrics. NMF and rNMF performed competitively on a few large-scale datasets

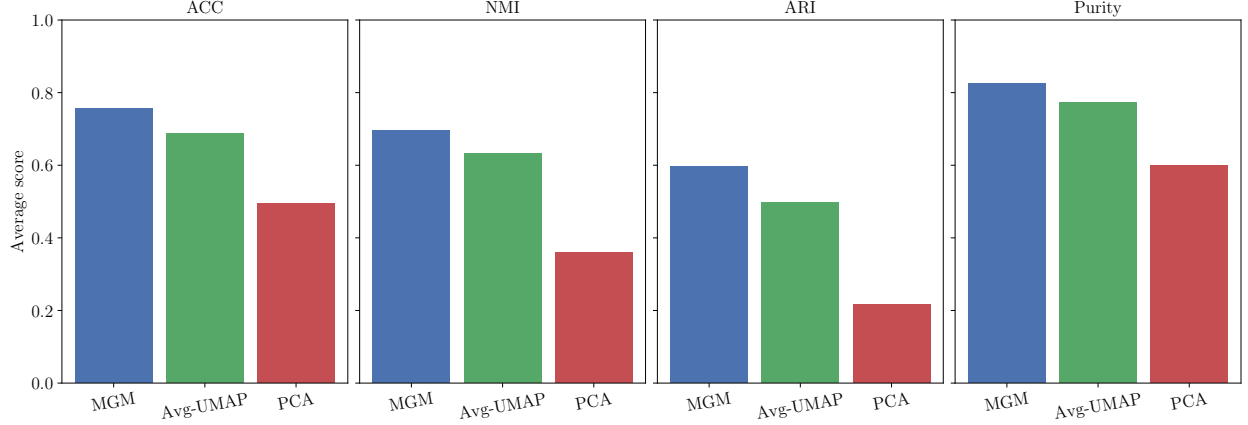


Figure 2: Average clustering performance across all datasets under the noisy condition (Setup I), comparing MGM, Avg-UMAP, and PCA. Panels correspond to four evaluation metrics: ACC, NMI, ARI, and Purity.

(e.g., GSE84133Human1 and GSE84133Human2), reflecting its strength in well-conditioned low-rank representations. Detailed results for each metric are presented in Tables 8–12, followed by averaged performance across all datasets in Figure 3 and qualitative visualization results in Figure 4.

Table 8: ACC under the refined condition (Setup II). Best in **bold**.

Dataset	MGM	NMF	rNMF	Avg-UMAP	PCA
GSE75748time	0.8776	0.6875 [20]	0.6873 [20]	0.8618	0.8327
GSE94820	0.9093	0.7189 [20]	0.7091 [20]	0.8598	0.5591
GSE67835	0.8843	0.8364 [20]	0.8357 [20]	0.7977	0.7390
GSE75748cell	0.9851	0.8006	0.8045	0.9693	0.8686
GSE109979	0.9780	0.7073	0.7073	0.9711	0.9311
GSE57249	0.9796	0.9796 [20]	0.9796 [20]	0.9642	0.5510
GSE84133human1	0.7490	0.7370 [20]	0.7988 [20]	0.6787	0.6451
GSE84133human2	0.6860	0.8994 [20]	0.8998 [20]	0.6609	0.7073
GSE84133human4	0.8910	0.8847 [20]	0.8847 [20]	0.8360	0.6431
Average ACC	0.8822	0.8057	0.8117	0.8444	0.7170

Table 9: NMI under the refined condition (Setup II). Best in **bold**.

Dataset	MGM	NMF	rNMF	Avg-UMAP	PCA
GSE75748time	0.8062	0.7244 [20]	0.7227 [20]	0.7958	0.8657
GSE94820	0.7862	0.6693 [20]	0.6624 [20]	0.7441	0.4859
GSE67835	0.8574	0.8017 [20]	0.7975 [20]	0.8063	0.6814
GSE75748cell	0.9592	0.8854	0.8897	0.9468	0.9229
GSE109979_329cell	0.9219	0.6321	0.6321	0.9003	0.8831
GSE57249	0.9293	0.9293 [20]	0.9293 [20]	0.4449	0.2270
GSE84133human1	0.7881	0.7949 [20]	0.8226 [20]	0.6773	0.5336
GSE84133human2	0.7519	0.8829 [20]	0.8835 [20]	0.7361	0.6347
GSE84133human4	0.8195	0.8694 [20]	0.8694 [20]	0.7949	0.4914
Average NMI	0.8466	0.7988	0.8010	0.7607	0.6362

Table 10: ARI under the refined condition (Setup II). Best in **bold**.

Dataset	MGM	NMF	rNMF	Avg-UMAP	PCA
GSE75748time	0.7350	0.5996 [20]	0.5969 [20]	0.7203	0.7470
GSE94820	0.7942	0.5556 [20]	0.5440 [20]	0.7317	0.3365
GSE67835	0.8214	0.7314 [20]	0.7295 [20]	0.7190	0.6253
GSE75748cell	0.9675	0.7479	0.7512	0.9403	0.8171
GSE109979	0.9428	0.5727	0.5727	0.9253	0.8834
GSE57249	0.9483	0.9483 [20]	0.9483 [20]	0.9145	0.1438
GSE84133human1	0.5987	0.6120 [20]	0.7080 [20]	0.5386	0.4289
GSE84133human2	0.5961	0.8929 [20]	0.8930 [20]	0.5684	0.5819
GSE84133human4	0.8245	0.8311 [20]	0.8311 [20]	0.7638	0.4031
Average ARI	0.8032	0.7213	0.7305	0.7580	0.5519

Table 11: Purity under the refined condition (Setup II). Best in **bold**.

Dataset	MGM	NMF	rNMF	Avg-UMAP	PCA
GSE75748time	0.8776	0.7455 [20]	0.7467 [20]	0.8634	0.8427
GSE94820	0.9093	0.7531 [20]	0.7429 [20]	0.8643	0.5607
GSE67835	0.9052	0.8719 [20]	0.8726 [20]	0.8748	0.7490
GSE75748cell	0.9851	0.8301	0.8310	0.9696	0.9016
GSE109979	0.9780	0.7073	0.7073	0.9711	0.9311
GSE57249	0.9796	0.9796 [20]	0.9796 [20]	0.9642	0.5755
GSE84133human1	0.8941	0.9099 [20]	0.9189 [20]	0.8813	0.6528
GSE84133human2	0.9153	0.9600 [20]	0.9602 [20]	0.9040	0.7291
GSE84133human4	0.9070	0.9412 [20]	0.9412 [20]	0.8870	0.6449
Average Purity	0.9279	0.8554	0.8556	0.9089	0.7319

Table 12: Avg-Purity under the refined condition (Setup II). Best in **bold**.

Dataset	MGM	NMF	rNMF	Avg-UMAP	PCA
GSE75748time	0.8546	0.8140	0.8138	0.8440	0.9116
GSE94820	0.8383	0.8211	0.8047	0.7981	0.8445
GSE67835	0.8452	0.7859	0.7409	0.7989	0.8819
GSE75748cell	0.9637	0.9260	0.9310	0.9519	0.9382
GSE109979	0.9557	0.8497	0.8497	0.9420	0.9459
GSE57249	0.9342	0.9342	0.9342	0.9154	0.6624
GSE84133human1	0.8685	0.8576	0.8584	0.8412	0.8583
GSE84133human2	0.7717	0.8897	0.8990	0.7508	0.8052
GSE84133human4	0.8594	0.9238	0.9238	0.8403	0.8656
Average Avg-Purity	0.8669	0.8617	0.8768	0.8536	0.8571

To consolidate these per-metric outcomes, Figure 3 reports the averages across the nine datasets for each metric, offering an at-a-glance comparison of the five methods.

Remark 4.1. *Results for NMF and rNMF under the metrics of ACC, NMI, ARI, and Purity are adopted*

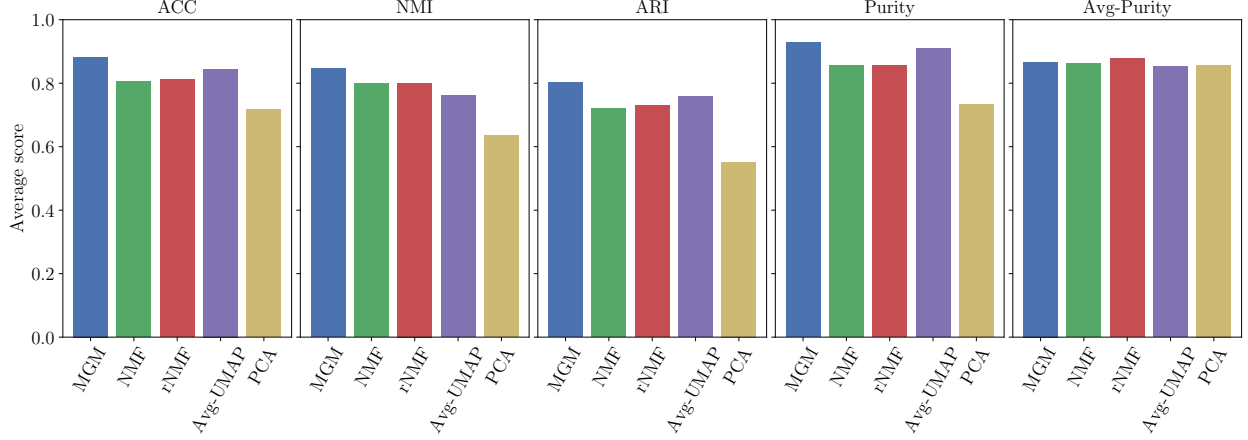


Figure 3: Average clustering performance under the refined condition (Setup II), comparing MGM, NMF, rNMF, Avg-UMAP, and PCA across five evaluation metrics (ACC, NMI, ARI, Purity, and Avg-Purity). Each panel shows the mean score of one metric across all datasets.

from [20], except for the datasets GSE75748cell and GSE109979, which were reproduced using the authors’ publicly available code, as these datasets were not reported in the original paper. For Avg-Purity, all results were independently computed in this study using the same publicly available implementation for consistency. For fair comparison, PCA results were obtained by performing clustering on embeddings reduced to the same dimensionality as that used in the proposed MGM framework.

Analysis. Across the five evaluation metrics: ACC, NMI, ARI, purity, and Avg-Purity, the proposed multiscale Grassmann manifolds (MGM) framework demonstrates strong and consistent performance under the refined condition (Setup II). As summarized in Tables 8–12, MGM achieves the highest overall mean values on four of the five metrics (ACC, NMI, ARI, and Purity). For Avg-Purity, MGM ranks second overall, only slightly below rNMF, with a marginal difference. This consistency across all metrics indicates that integrating multiscale geometric information within the Grassmann manifold yields stable and competitive clustering representations even after refined preprocessing. A closer examination of the dataset-wise results shows that MGM achieves the best or comparable performance on the majority of datasets, particularly those of small and medium scale, including GSE75748time, GSE94820, GSE67835, GSE75748cell, GSE109979, and GSE57249. In these datasets, MGM consistently attains top scores across multiple metrics, highlighting its advantage in preserving multiscale structure and local manifold geometry. This suggests that the subspace-based representation on the Grassmann manifold is especially effective when the number of cells is limited or residual noise remains after preprocessing. For the larger datasets (GSE84133human1, GSE84133human2, and GSE84133human4), NMF slightly surpasses MGM on certain metrics, likely because factorization-based methods capture broader global relationships in complex, high-dimensional data. Nevertheless, MGM still outperforms PCA and Avg-UMAP across all metrics and remains highly competitive with NMF and rNMF overall.

Finally, to complement the quantitative evaluation, Figure 4 presents a direct visual comparison of the embeddings generated by the proposed multiscale Grassmann manifolds (MGM) framework, PCA→UMAP (i.e., applying UMAP on features that have been first reduced in dimension using PCA), and standard UMAP computed directly on the preprocessed data.

Observation. In Figure 4, across the five representative datasets, the MGM embeddings consistently produce clearer inter-cluster separation and more compact group structures compared with PCA→UMAP and UMAP. In particular, the MGM results for GSE75748cell and GSE109979 show well-defined and isolated clusters, whereas PCA→UMAP retains partial overlap between groups and UMAP exhibits widespread dispersion with blurred boundaries. For GSE67835 and GSE75748time, MGM preserves global organization while maintaining distinct local partitions, indicating that the Grassmann manifold representation enhances

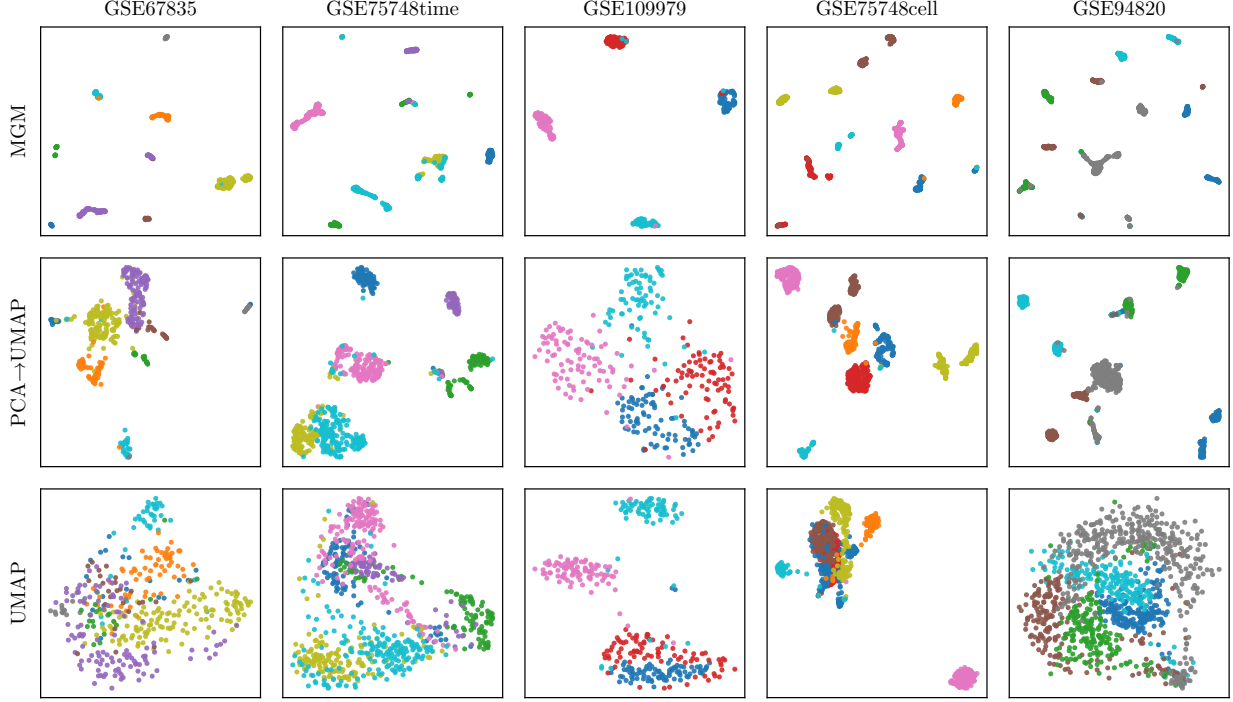


Figure 4: Visualization under UMAP (MGM vs. PCA→UMAP vs. UMAP). Columns correspond to datasets (GSE67835, GSE75748time, GSE109979, GSE75748cell, GSE94820), and rows correspond to methods. Top row: MGM, where chordal distances are computed from multiscale subspace representations and then embedded using UMAP with a precomputed metric. Middle row: PCA→UMAP, obtained by applying UMAP to PCA-reduced features using the Euclidean metric. Bottom row: UMAP, obtained directly from the preprocessed data without PCA or Grassmann manifold representation.

multiscale consistency. On GSE94820, MGM better preserves between-group separation, whereas PCA and UMAP fail to disentangle nearby populations. Overall, these visual results confirm the quantitative findings in Figure 3, showing that the MGM framework provides the most balanced representation, effectively enhancing separability while maintaining stable global structure across diverse single-cell datasets.

Remark 4.2. All visualizations in Figure 4 are generated under the parameter settings of Setup II. Both MGM and PCA→UMAP are constructed using features reduced to 50 dimensions by PCA, ensuring that the comparison focuses on the effect of the representation framework rather than differences in input dimensionality. The neighborhood size in UMAP is set to its default value of 15.

5 Discussion

The experimental results in Section 4 demonstrate that the proposed multiscale Grassmann manifolds (MGM) framework provides stable and competitive clustering performance across a broad range of single-cell datasets. It performs particularly well on small and moderately sized datasets, where it is competitive with NMF, while maintaining comparable performance on larger datasets. To further clarify the behavior of MGM under different scale conditions, two representative examples are examined in the Supporting Information (Section 2.1 and Section 2.2).

Section 2.1 in the Supporting Information presents the GSE57249 dataset, where all scales yield consistently high-quality single-scale UMAP embeddings. In this uniform condition, MGM preserves the discriminative structure without degradation and maintains results comparable to the best single-scale configuration, slightly improving over the average UMAP score. This observation suggests that aggregating subspaces on the Grassmann manifold does not blur or weaken well-formed local relationships when the underlying scales are uniformly strong.

Section 2.2 in the Supporting Information presents the GSE84133Human2 dataset, where different scales produce variable UMAP embeddings, and some large-scale settings are affected by noise and over-smoothing. In this noisy condition, MGM combines information from both effective and weak scales to form a more stable subspace representation. It shows higher accuracy and information-based metrics than the average UMAP result and sometimes performs better than the best single-scale case. This suggests that Grassmann manifold integration helps maintain robustness when individual scales do not perform well.

Together, the two cases highlight the essential advantage of the proposed framework. MGM can retain discriminative information under uniformly good scales while compensating for instability under noisy or heterogeneous conditions. This dual robustness underscores the potential of multiscale Grassmann manifold learning. Although the present implementation relies on a simple power-based sampling of scale sizes, the observed improvements suggest that more adaptive or data-driven scale selection strategies could further strengthen its capability in handling diverse single-cell datasets.

In this study, we demonstrated the effectiveness of the proposed multiscale Grassmann manifolds (MGM) framework using UMAP as a representative dimensionality reduction method. Nevertheless, the framework itself is general and can be readily combined with a wide range of existing algorithms, including t-SNE [31], NMF [18, 26], MCIST [14], and CCP-assisted methods [20]. By providing a unified geometric formulation for integrating multiscale information, the MGM framework establishes a flexible foundation that can be extended to other manifold learning or matrix factorization models. We anticipate that future studies will explore these directions, further advancing the application of Grassmann manifold representations in single-cell data analysis and beyond.

6 Conclusion

The proposed framework is designed to be general rather than specific to a single algorithm. While UMAP was used here to illustrate its feasibility, the multiscale Grassmann manifolds (MGM) formulation can be seamlessly integrated with other dimensionality reduction and representation learning methods, such as t-SNE [31], NMF [20, 26], MCIST [14], and CCP-assisted approaches [19]. By representing multiscale embeddings as points on the Grassmann manifold, the framework captures structural consistency across scales and provides a unified non-Euclidean representation for complex, high-dimensional data. Experiments on nine benchmark single-cell RNA-seq datasets demonstrated that MGM achieves competitive clustering performance compared with conventional Euclidean and manifold-based approaches, particularly on small to medium-sized datasets where scale variability and noise have stronger effects.

Future research may extend this framework toward adaptive or data-driven scale selection and more efficient subspace construction to improve robustness and scalability on large or heterogeneous datasets. Beyond single-cell analysis, the same formulation can be applied to other high-dimensional domains, offering a general pathway for integrating multiscale information through geometric modeling. Overall, the MGM framework establishes a principled and extensible foundation for multiscale geometric learning, supporting broader applications of Grassmann manifold representations in biological and computational data science.

Data and Code Availability

All source code is available at <https://github.com/XiangXiangJY/MGM>, and the single-cell dataset pre-processing scripts are adapted from <https://github.com/hozumiyu/TopologicalNMF-scRNAseq>.

Supporting Information

Additional materials, including complete parameter configurations for Setup I and Setup II, supplementary experimental analyzes, clustering settings, and detailed definitions of the evaluation metrics, are provided in the Supporting Information at <https://github.com/XiangXiangJY/MGM>.

Acknowledgments

This work was supported in part by NIH grant R35GM148196, National Science Foundation grant DMS2052983, Michigan State University Research Foundation, and Bristol-Myers Squibb 65109.

References

- [1] P.-A. Absil, R. Mahony, and R. Sepulchre. Riemannian geometry of Grassmann manifolds with a view on algorithmic computation. *Acta Appl. Math.*, 80(2):199–220, 2004.
- [2] Maayan Baron, Adrian Veres, Samuel L Wolock, Andrea L Faust, Renaud Gaujoux, Adrian Vetere, Jaemin H Ryu, Bridget K Wagner, Shai S Shen-Orr, Allon M Klein, Douglas A Melton, and Itai Yanai. A single-cell transcriptomic map of the human and mouse pancreas reveals inter- and intra-cell population structure. *Cell Systems*, 3(4):346–360.e4, 2016.
- [3] E. Batzies, K. Hüper, L. Machado, and F. Silva Leite. Geometric mean and geodesic regression on Grassmannians. *Linear Algebra Appl.*, 466:83–101, 2015.
- [4] Etienne Becht, Leland McInnes, John Healy, Charles-Antoine Dutertre, Immanuel WH Kwok, Lai Guan Ng, Florent Gehrmann, and Evan W Newell. Dimensionality reduction for visualizing single-cell data using umap. *Nature biotechnology*, 37(1):38–44, 2019.
- [5] Thomas Bendokat, Ralf Zimmermann, and P-A Absil. A Grassmann manifold handbook: Basic geometry and computational aspects. *Advances in Computational Mathematics*, 50(1):6, 2024.
- [6] Fernando H Biase, Xi Cao, and Sheng Zhong. Cell fate inclination within 2-cell and 4-cell mouse embryos revealed by single-cell rna sequencing. *Genome Research*, 24(11):1787–1796, 2014.
- [7] Rasmus Bro and Age K Smilde. Principal component analysis. *Analytical methods*, 6(9):2812–2831, 2014.
- [8] Zixuan Cang, Yanxiang Zhao, Axel A Almet, Adam Stabell, Raul Ramos, Maksim V Plikus, Scott X Atwood, and Qing Nie. Screening cell-cell communication in spatial transcriptomics via collective optimal transport. *Nature methods*, 20(2):218–228, 2023.
- [9] Rudrasis Chakraborty and Baba C Vemuri. Recursive frechet mean computation on the grassmannian and its applications to computer vision. In *Proceedings of the IEEE International Conference on Computer Vision*, pages 4229–4237, 2015.
- [10] Duan Chen, Shaoyu Li, and Xue Wang. Geometric structure guided model and algorithms for complete deconvolution of gene expression data. *Foundations of data science (Springfield, Mo.)*, 4(3):441, 2022.
- [11] Yoon Ha Choi and Jong Kyoung Kim. Dissecting cellular heterogeneity using single-cell rna sequencing. *Molecules and cells*, 42(3):189–199, 2019.
- [12] Li-Fang Chu, Ning Leng, Jue Zhang, Zhonggang Hou, Daniel Mamott, David T Vereide, Jee Choi, Christina Kendzioriski, Ron Stewart, and James A Thomson. Single-cell rna-seq reveals novel regulators of human embryonic stem cell differentiation to definitive endoderm. *Genome biology*, 17(1):173, 2016.

- [13] Sean Cottrell, Yuta Hozumi, and Guo-Wei Wei. K-nearest-neighbors induced topological pca for single cell rna-sequence data analysis. *Computers in biology and medicine*, 175:108497, 2024.
- [14] Sean Cottrell and Guo-Wei Wei. Multiscale cell-cell interactive spatial transcriptomics analysis. *Research Square*, pages rs–3, 2025.
- [15] David F Crouse. On implementing 2d rectangular assignment algorithms. *IEEE Transactions on Aerospace and Electronic Systems*, 52(4):1679–1696, 2016.
- [16] Spyros Darmanis, Steven A Sloan, Ye Zhang, Martin Enge, Christine Caneda, Lawrence M Shuer, Melanie G Hayden Gephart, Ben A Barres, and Stephen R Quake. A survey of human brain transcriptome diversity at the single cell level. *Proceedings of the National Academy of Sciences*, 112(23):7285–7290, 2015.
- [17] Alan Edelman, Tomás A Arias, and Steven T Smith. The geometry of algorithms with orthogonality constraints. *SIAM journal on Matrix Analysis and Applications*, 20(2):303–353, 1998.
- [18] Hongsong Feng, Sean Cottrell, Yuta Hozumi, and Guo-Wei Wei. Multiscale differential geometry learning of networks with applications to single-cell rna sequencing data. *Computers in biology and medicine*, 171:108211, 2024.
- [19] Yuta Hozumi and Guo-Wei Wei. Analyzing scrna-seq data by ccp-assisted umap and tsne. *PloS one*, 19(12):e0311791, 2024.
- [20] Yuta Hozumi and Guo-Wei Wei. Analyzing single cell rna sequencing with topological nonnegative matrix factorization. *Journal of Computational and Applied Mathematics*, 445:115842, 2024.
- [21] Lawrence Hubert and Phipps Arabie. Comparing partitions. *Journal of classification*, 2(1):193–218, 1985.
- [22] Tram Huynh and Zixuan Cang. Topological and geometric analysis of cell states in single-cell transcriptomic data. *Briefings in Bioinformatics*, 25(3):bbae176, 2024.
- [23] Songrun Jiang, Chunyan Wang, Qiucheng Sun, and Zhi Zhang. A robust multi-scale clustering framework for single-cell rna-seq data analysis. *Scientific Reports*, 15(1):18543, 2025.
- [24] Abhishek Kumar, Piyush Rai, and Hal Daume. Co-regularized multi-view spectral clustering. *Advances in neural information processing systems*, 24, 2011.
- [25] Serge Lang. *Fundamentals of Differential Geometry*, volume 191 of *Graduate Texts in Mathematics*. Springer-Verlag, New York, 1999.
- [26] Daniel D Lee and H Sebastian Seung. Learning the parts of objects by non-negative matrix factorization. *nature*, 401(6755):788–791, 1999.
- [27] Danping Li, Lei Wang, Zhong Xue, and Stephen TC Wong. When discriminative k-means meets grassmann manifold: disease gene identification via a general multi-view clustering method. In *2016 IEEE-EMBS International Conference on Biomedical and Health Informatics (BHI)*, pages 364–367. IEEE, 2016.
- [28] Sijie Li, Heyang Hua, and Shengquan Chen. Graph neural networks for single-cell omics data: a review of approaches and applications. *Briefings in Bioinformatics*, 26(2), 2025.
- [29] Xiaoguang Li, Tao Zhou, Xingdong Feng, Shing-Tung Yau, and Stephen S-T Yau. Exploring geometry of genome space via grassmann manifolds. *The Innovation*, 5(5), 2024.
- [30] Junjie Lu, Anna Baccei, Edroaldo Lummertz da Rocha, Christelle Guillermier, Sean McManus, Lydia A Finney, Cheng Zhang, Matthew L Steinhauser, Hu Li, and Paul H Lerou. Single-cell rna sequencing

- reveals metallothionein heterogeneity during hesc differentiation to definitive endoderm. *Stem cell research*, 28:48–55, 2018.
- [31] Laurens van der Maaten and Geoffrey Hinton. Visualizing data using t-sne. *Journal of machine learning research*, 9(Nov):2579–2605, 2008.
 - [32] James B McQueen. Some methods of classification and analysis of multivariate observations. In *Proc. of 5th Berkeley Symposium on Math. Stat. and Prob.*, pages 281–297, 1967.
 - [33] Andrew Ng, Michael Jordan, and Yair Weiss. On spectral clustering: Analysis and an algorithm. *Advances in neural information processing systems*, 14, 2001.
 - [34] KVSN Rama Rao and B Manjula Josephine. Exploring the impact of optimal clusters on cluster purity. In *2018 3rd International Conference on Communication and Electronics Systems (ICCES)*, pages 754–757. IEEE, 2018.
 - [35] Yiming Ren and Guowei Wei. Interpretability and representability of commutative algebra, algebraic topology, and topological spectral theory for real-world data. *arXiv preprint arXiv:2510.20973*, 2025.
 - [36] Duluxan Sritharan, Shu Wang, and Sahand Hormoz. Computing the riemannian curvature of image patch and single-cell rna sequencing data manifolds using extrinsic differential geometry. *Proceedings of the national academy of sciences*, 118(29):e2100473118, 2021.
 - [37] Zhe Su, Yiyong Tong, and Guo-Wei Wei. Hodge decomposition of single-cell rna velocity. *Journal of chemical information and modeling*, 64(8):3558–3568, 2024.
 - [38] Faisal Suwayyid, Yuta Hozumi, Hongsong Feng, Mushal Zia, JunJie Wee, and Guo-Wei Wei. Cakl: Commutative algebra k-mer learning of genomics. *arXiv preprint arXiv:2508.09406*, 2025.
 - [39] Aarthi Venkat, Dhananjay Bhaskar, and Smita Krishnaswamy. Multiscale geometric and topological analyses for characterizing and predicting immune responses from single cell data. *Trends in Immunology*, 44(7):551–563, 2023.
 - [40] Alexandra-Chloé Villani, Rahul Satija, Gary Reynolds, Siranush Sarkizova, Karthik Shekhar, James Fletcher, Morgane Griesbeck, Andrew Butler, Shiwei Zheng, Suzan Lazo, et al. Single-cell rna-seq reveals new types of human blood dendritic cells, monocytes, and progenitors. *Science*, 356(6335):eaah4573, 2017.
 - [41] Nguyen Xuan Vinh, Julien Epps, and James Bailey. Information theoretic measures for clusterings comparison: is a correction for chance necessary? In *Proceedings of the 26th annual international conference on machine learning*, pages 1073–1080, 2009.
 - [42] Osamu Yamaguchi, Kazuhiro Fukui, and K-i Maeda. Face recognition using temporal image sequence. In *Proceedings third IEEE international conference on automatic face and gesture recognition*, pages 318–323. IEEE, 1998.
 - [43] Chen-Min Yang, Dong Huang, Yuan-Kun Xu, Xiuting He, Guang-Yu Zhang, and Chang-Dong Wang. Towards multi-fusion graph neural network for single-cell rna sequence clustering. *Neurocomputing*, 631:129764, 2025.
 - [44] Murong Yang, Shihui Ying, Xin-Jian Xu, and Yue Gao. Multi-view spectral clustering on the grassmannian manifold with hypergraph representation. *arXiv preprint arXiv:2503.06066*, 2025.
 - [45] Ke Ye and Lek-Heng Lim. Schubert varieties and distances between subspaces of different dimensions. *SIAM Journal on Matrix Analysis and Applications*, 37(3):1176–1197, 2016.